

34 1. Introduction

35 Mycotoxins are naturally occurring toxins produced by certain mold species. The main fungal genera
36 producing the mycotoxins include *Aspergillus*, *Fusarium*, and *Penicillium*. The most common
37 mycotoxins are aflatoxins, OTA, fumonisins, deoxynivalenol, T-2 toxin, and zearalenone ¹. The
38 mycotoxins are present at all stages of the food chain and can be found in products such as meat, fruits,
39 wine, beer, coffee, tea, milk, nuts, dried fruits, cereals, and many more. Additionally, these compounds
40 exhibit high chemical stability. Their crystallization state and high resistance to high temperatures or
41 even gamma radiation ² make them insensitive to conventional sterilization methods. On the other hand,
42 chemical products that are able to neutralize their toxic effect are often causing other health problems.

43 Among the mycotoxins listed above, OTA is recognized as one of the most toxic and has been classified
44 as a group I carcinogen. Although the toxicity of OTA has been studied for many years, its complex
45 mechanism of action has not been elucidated in detail yet. However, based on *in vitro* and animal studies,
46 this toxin is 'this time was as carcinogenic, teratogenic, hepatotoxic, neurotoxic, and immunotoxic.

47 OTA is also known to generate covalent DNA adducts and to promote oxidative DNA damage based on
48 the production of reactive oxygen species ³. DNA is of key importance in the molecular processes of all
49 living organisms. Therefore, exploring the OTA–DNA interaction mechanisms is of great importance—
50 first, to understand the exact DNA damage mechanism, and second, to develop the therapeutic drugs in
51 the future. Throughout the years, DNA has been reported as a target molecule of various drugs and toxic
52 compounds, which can lead to a change in DNA structures and genetic mutations. Molecules can interact
53 with DNA in three different ways. First, through the intercalation between the DNA base pairs, which is
54 the most effective and thus destructive one; second, through the groove binding; and the last one, through
55 the electrostatic interactions.

56 To study the interaction mechanisms of small molecules with DNA, several techniques have been
57 utilized and reported, i.a. fluorescence spectroscopy ⁴, UV-spectrophotometry ⁵, circular dichroism ⁶,
58 mass spectrometry ⁷, molecular docking ⁵, and electrochemical methods ⁶. Moreover, techniques like
59 competitive displacement, iodide quenching effect, viscosity measurements, and DNA melting assays
60 have been used for further identification of the binding mode.

61 According to the literature, the mycotoxins have already been grafted on a few different surfaces. ⁸. In
62 our experiment, we used a nanodiamond surface with COOH functional groups, previously studied by
63 Tian *et al.* ⁹. The surface coverage, according to *ab-initio* calculations for COOH presented in ⁹, is
64 approximately 6%. The carboxylated nanodiamonds (NDs) are efficient fluorescent agents enabling
65 grafting various surface species ¹⁰ or interacting with biomatter ¹¹. The fields of physics and biology
66 have discovered nanodiamond as an ideal material for at least two very different scientific applications.
67 Biologists, on the one hand, have found that diamond nanoparticles show promise as exceptionally
68 robust fluorescent dyes, with many potential applications in biolabeling ^{12,13}. On the other hand,

69 physicists have made tremendous progress in understanding and controlling the electronic properties of
70 vacancy^{12,14}. Before introducing the nitrogen-vacancy (NV) center in nanodiamond and its use for
71 nanoscale sensing, we note that several excellent reviews have appeared highlighting different aspects
72 of diamond nanoparticles and NV centers. Jelezko & Wrachtrup¹⁵ have given an early overview of NV
73 centers in diamond. More detailed descriptions of photoelectric detection and quantum readout of the
74 NV center have been given by Bourgeois et al.¹⁶. Chi-Cheng Fu et al.¹⁷ have provided an overview of
75 the nanodiamonds as fluorescent cellular biomarkers.

76 NV centers in the nanodiamonds are atomic-level defects which display a remarkable range of
77 properties, including sustained fluorescence, long quantum coherence times under ambient conditions,
78 and demonstrated biocompatibility¹⁸⁻²⁰. The nanodiamonds containing negatively charged NV centers
79 have proven to be a promising tool in bio labeling, biomarking²¹. Recently, an important element of
80 nanodiamonds has been surface functionalization²².

81 In this work, we have explored interactions between calf thymus DNA (ct DNA) and OTA grafted at the
82 fluorescent nanodiamond's surface. To date, fluorescent nanodiamonds have been used only as a sorbent
83 / carrier of the mycotoxins to facilitate their removal from an organism and to neutralize their toxic effect
84^{23,24}. Thanks to NDs tailored chemistry, OTA has been immobilized stably on the NDs' surface during
85 experiment conduction. The OTA immobilization density and stability were also revealed by *ab-initio*
86 simulations at the diamond [111] surface covered with 6% of carboxyl linkers.

87 Furthermore, the immobilization of OTA has been performed in a few, widely available drinks,
88 beverages, and liquids to assess the influence of the environment on OTA toxicity. What is more,
89 complex of the OTA and NDs enables the investigations of the DNA-OTA interactions using both
90 fluorescence and UV-Vis spectroscopy.

91

92 **2. Experimental**

93 *2.1. Materials*

94 Carboxylated, fluorescent nanodiamonds with an average size of 750 nm, purchased from Adámas
95 Nanotechnologies, USA have been chosen as substrates for immobilization of OTA. The Ochratoxin A
96 from *Aspergillus ochraceus* has been received from Sigma-Aldrich, Poland. The stock solution of ct
97 DNA has been obtained from Sigma Aldrich, Poland

98 Both OTA and ct DNA have been stored in phosphate buffer saline (PBS; pH=7.4) containing 140 mM
99 of sodium chloride (NaCl), 2.7 mM of potassium chloride (KCl), 0.1 mM of sodium phosphate dibasic
100 (Na₂HPO₄), and 1.8 mM of potassium phosphate monobasic (KH₂PO₄), all of which have been supplied
101 by Sigma-Aldrich, Poland. OTA was suspended in PBS at 1 mg/mL concentration and stored as aliquots
102 at -20°C. The ct DNA has been suspended in 0.01 M PBS, and its concentration was determined using
103 UV-Vis spectroscopy based on the UV absorbance measurement at 260 nm using a molar extinction
104 coefficient of 6600 M⁻¹cm⁻¹.

105 For immobilization of OTA on the nanodiamonds' surfaces, the following chemicals have been selected:
106 4-aminophenylacetic acid, N-hydroxysuccinimide (NHS), 1-ethyl-3-(3-dimethylaminopropyl)-
107 carbodiimidehydrochloride (EDC), potassium ferricyanide ($K_3[Fe(CN)_6]$), potassium ferrocyanide
108 ($K_4[Fe(CN)_6]$), dimethylsulfoxide (DMSO), sulfuric acid (H_2SO_4) (98%), and ethanol (98%). All of the
109 chemicals listed above have been supplied by Sigma-Aldrich, Poland.

110 For the assessment of an impact of a liquid environment on OTA's interaction with ct DNA, the
111 following comestibles have been selected: 10% spirit vinegar, 100% lemon juice, 100% apple juice, and
112 green tea. Deionized water has been used as a reference. Detailed information on pH, and the origins of
113 the comestible liquids is summarized in **Table 1**.

114

115 **Table 1.** Origins, and values of pH of the comestible liquids used in the experiment.

Comestible liquid	pH	Manufacturer
Spirit vinegar, 10%	2.38	OCTIM Sp. z o.o., Poland
Lemon juice, 100%	2.55	Polenghi LAS s.r.l., Italy
Apple juice, 100%	3.51	Tymbark - MWS Sp. z o.o. Sp.k., Poland
Green tea	7.10	Unilever Polska Sp. z o.o., Poland

116

117 2.2. Experimental Procedure

118 The nanodiamonds were separately suspended in every one of the 4 comestible liquids, and in deionized
119 water. A concentration of the diamond in the suspensions was 0.1% (w/w). To ensure a repeatability of
120 the samples, the following procedure for the tea brewing has been established: one sachet bag of the
121 green tea was poured with 250 mL of filtered, boiling water, and removed after exactly 5 minutes. Before
122 OTA was immobilized on the nanodiamonds' surfaces, the suspensions were being homogenized in an
123 ultrasonic bath (Polsonic Sonic-3, 40 kHz) for 30 min.

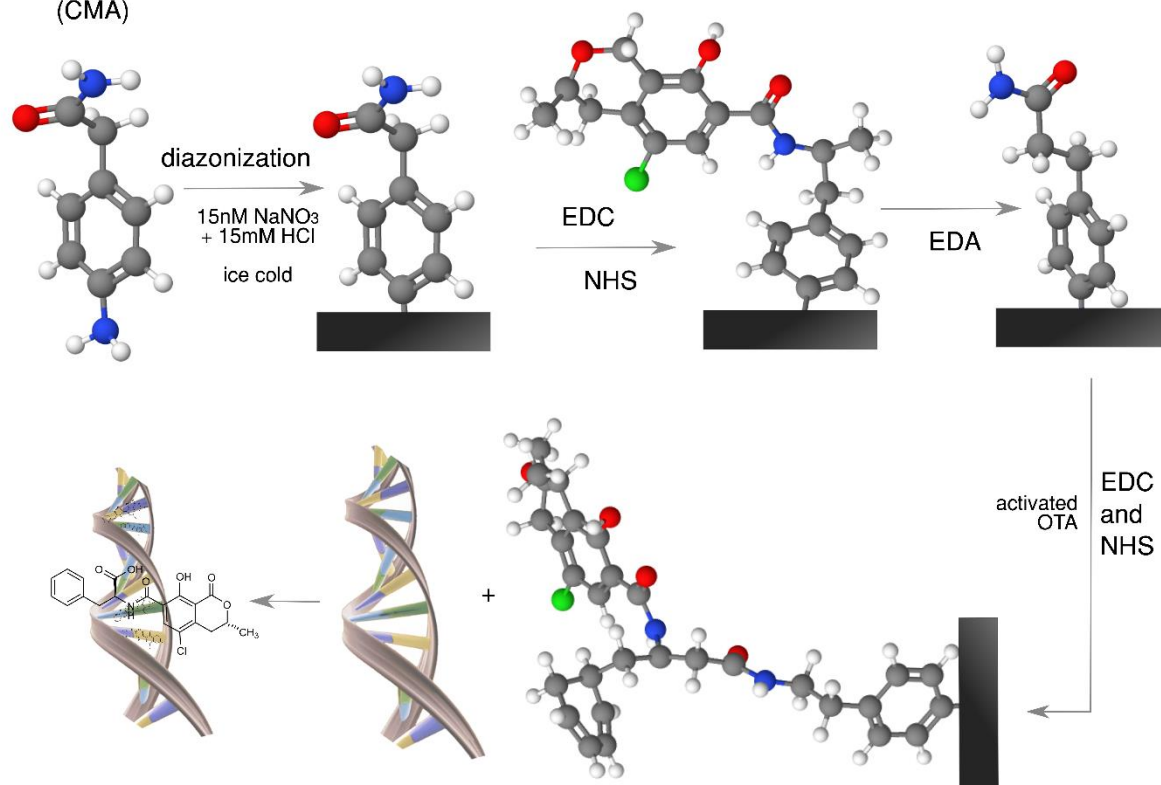
124 In the present study, OTA was directly immobilized to 4-carboxymethylaniline (CMA). The proposed
125 reaction scheme (**Figure 1**) consists of an activation of carboxyl groups on OTA with EDC/NHS, and a
126 crosslinking of the activated carboxyl groups to amine groups generated on CMA-coated
127 nanodiamonds' surfaces. First, 10 mg of 4-carboxymethylaniline (CMA) were activated in the presence
128 of 20.5 mg of EDC, and 11.5 mg of NHS in 1 mL of PBS for 30 min with stirring. After the activation,
129 carboxylic acid terminal moieties of CMA were converted to amine groups during incubation with 1 M
130 ethylenediamine (EDA), pH 8.5 for 7 min. Free carboxylic groups were blocked with 1 M ethanolamine
131 (EOA), pH 8.5, during incubation lasting 2 min.

132 After OTA was attached to the surfaces of the nanodiamonds, its interaction with ct DNA was
133 investigated by means of UV-Vis spectroscopy, fluorescence spectroscopy, and analysis of zeta
134 potential.

135



4-carboxymethyl aniline
(CMA)



136

137 **Figure 1.** Scheme of nanodiamond modification by OTA and graphical representation of DNA-OTA
138 interactions.

139 2.3. Apparatus

140 A high-precision quartz glass cuvette with outer dimensions of 45 × 12.5 × 12.5 mm and an optical path
141 length of 10 mm has been used to analyze the UV-Vis absorption, and the fluorescence of the samples.
142 All the absorption spectra were recorded in 250–650-nm range with the Perkin Elmer Lambda 35 UV–
143 Vis spectrometer equipped with the integrating sphere module for reflectance measurements.

144 The fluorescence spectra were measured using a custom-made setup with 532 nm CW Nd:YAG SHG
145 laser (Millenia, Spectra Physics) as an excitation source. The spectra were analyzed using 0.3 m
146 monochromator (SR303i, Andor) equipped with 600 groves/mm grating and recorded with ICCD
147 detector (DH740, Andor). The samples were excited by the laser from the front at 45° angle. The
148 fluorescence signal was collected using the quartz lens end focused on the entrance of optical fiber. In
149 the detection path the band-pass filter (OG570, Schott) was used to block the laser radiation.

150 The electrical properties (conductivity and zeta potential) of the samples were measured using the
151 Zetasizer Nano ZS (Malvern Panalytical, UK) particle analyzer equipped with a high concentration cell.

152

153 2.4. Measurement Procedures

154 In the analysis of both the UV-Vis absorption, and the fluorescence, an empty cuvette was measured
155 first to register a background signal, which would later be subtracted from the spectra of the samples.

156 Next, 2 mL of the suspension of OTA-immobilized nanodiamonds were placed in the cuvette and
157 analyzed. Then, the suspension of ct DNA was added portion-wise to the suspension present in the
158 cuvette. The following volumes of ct DNA suspension in total were added to the cuvette: 20 μL , 40 μL ,
159 60 μL , 80 μL , 100 μL , 150 μL , 200 μL , 500 μL . After each portion of the ct DNA suspension was added,
160 the sample was vortexed (VELP Scientifica TX4) for 10 sec at 400 rpm, and then left for 5 minutes,
161 after which the absorption and fluorescence measurements were carried out.

162 The conductivity and the zeta potential of the samples were examined at 25°C at three stages of
163 modification of the nanodiamonds: after the nonmodified nanodiamonds were dispersed in the liquids
164 in 0.1% concentration; after OTA was immobilized on their surfaces; and finally after the addition of
165 500 μL of the solvent containing ds ct DNA to 2 mL of the suspensions of the OTA-modified
166 nanodiamonds.

167

168 *2.5 Ab-initio and Molecular Dynamics Simulation of ND-OTA Complexes*

169 The *ab-initio* simulations were conducted on the [111] oriented diamond slab containing 4950 carbon
170 atoms (9 layers, each containing 550 atoms). Model was created using the Atomistix Tool Kit
171 Quantumwise²⁵ (ATK, Synopsys, USA). The diamond slab was terminated by COOH groups with
172 covalently grafted OTA. The thickness of the slab was 19.6 Å. The model is assumed to be an infinite
173 plane; on the borders of supercell the periodic boundary conditions were applied. To leave sufficiently
174 large space for the adsorbing molecules and analyze interaction with images, the 6.8 nm vacuum buffer
175 was added above the surface. Periodic boundary conditions were applied in the unit cell, while the ratios
176 between atom types within the cell were kept similar for the entire surface.

177 The [111] diamond surface consists of 225 surficial carbon atoms, where each of the carbon atoms forms
178 three bonds with other carbons. Priorly, hydrogen atoms are bonded to each carbon atom resulting in
179 the 100% hydrogen termination. If the single hydrogen atom is removed, the surface gets radical site
180 (per unit cell). Radical site could be saturated by the COOH (or OTA), then the percental coverage
181 changes to $1/225 \approx 0.44\%$. Surface coverage is usually estimated in reference to all possible radical sites
182 on the given surface, regardless the occupation. Such a convention was already used in the papers
183 describing surface chemistry simulations⁹. Large molecules such as OTA could cover up the diamond
184 surface which is already covered by relatively small atoms such as H enabling the intersection of the
185 covered areas. This phenomenon does not impact the percentage coverage, which is independent of the
186 molecule geometrical size. Models used in Force-Field and density-functional theory (DFT) calculations
187 have different cell sizes but similar percentage coverages of COOH and OTA. During all Force-Field
188 calculations on the diamond surface, 13 COOH species were present corresponding to 5.77% coverage.

189 The applied ochratoxin structure was downloaded from the PubChem²⁶ databases (CID 442530). The
190 binding to the diamond surface was conducted to reproduce the mechanism presented in **Figure 1**. Six



191 separated slabs were designed containing perpetually increased number of OTA molecules bounded to
192 diamond surface, from one to six per chosen area (see **Figure 2**). The binding energy E_{bind} of the model
193 system can be calculated using the formula (1).

$$194 \quad E_{bind} = \frac{1}{n}(E_{slab+OTA} - E_{slab} - nE_{OTA}) \quad (1)$$

195 Where $E_{slab+OTA}$ is the total energy of the system with OTA and all terminating species, E_{slab} is the
196 energy of the system without OTA (the radical sites created by removing OTA are left passivated), and
197 E_{OTA} is the energy of one isolated OTA species. Small n denotes the number of OTA molecules in the
198 supercell.

199 To describe the energy of the system, the ATK Force-Field has been used. This module describes the
200 interatomic integration using the classical potentials set. This implementation is described elsewhere²⁷.
201 To calculate the operating forces, the reactive force field ReaxFF_CHONSMgPNaCuCl_2018_08 was
202 used²⁸. Before the total energy calculation, the atomic positions and the cell size were optimized based
203 on the Broyden-Fletcher-Goldfarb-Shanno (LBFGS) algorithm. The maximal force in the structure after
204 optimization did not exceed 0.05 eV/Å.

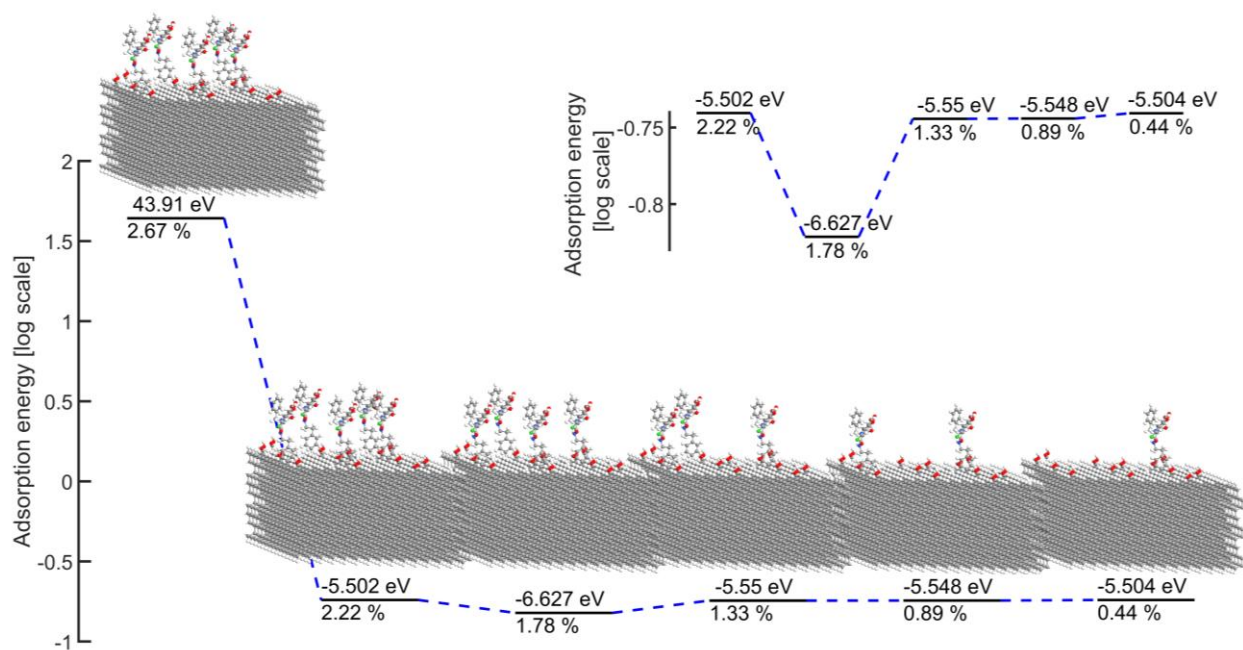
205 The diamond slab containing single OTA was applied for *ab-initio* band structure simulations by means
206 of DFT. The Quantum ATK toolbox enables conduction of such calculations based on a couple of
207 variants. The Linear Combination of Atomic Orbitals²⁹ (LCAO) was used to calculate electron density
208 functionals. To solve the matrix equations of the LCAO method, self-consistent field (SCF) iterations
209 were performed. The density mesh cut-off energy was set to 125 Hartree and k-point sampling utilizing
210 MonkhorstPack scheme was 3x2x1. During DFT calculation, the exchange-correlation of electrons was
211 included using GGA method with PBE (Perdew, Burke and Ernzerhof) functionals. The PseudoDojo³⁰
212 pseudopotentials with medium basis set were utilized to calculate the electron wave functions. The
213 detailed description of the mentioned basis set can be found in the paper of Smidstrup *et al.* (appendix)
214³¹.

215

216 **3. Results and Discussion**

217 *3.1. Simulations of the Adsorption Energy Dependence on the Surface Coverage*

218 The series of numerical studies were carried out to estimate the dependence of OTA adsorption energy
219 on the ND surface. The key aspect of this calculation was to estimate energetically favorable OTA
220 coverage density. The OTA coverage density and adsorption energies are plotted in **Figure 2**.



221

222 **Figure 2.** The binding energy for a series of [111] diamond models with different OTA concentration
 223 on the surface.

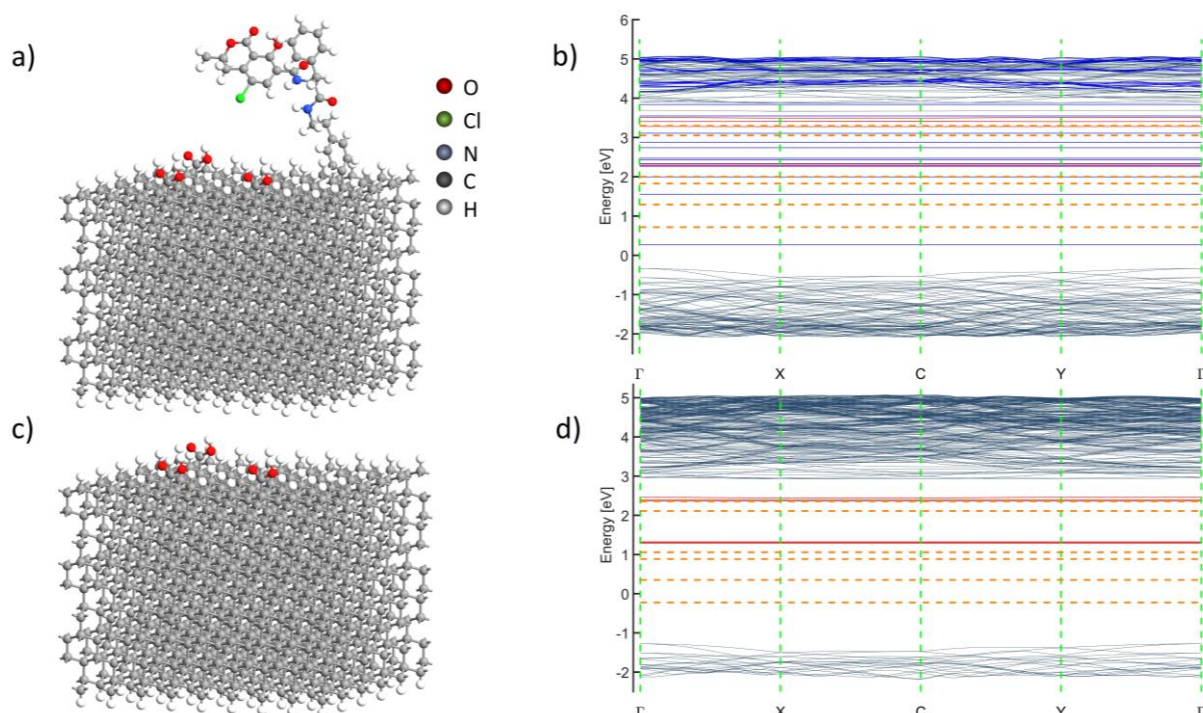
224 According to Force-Field calculation, the energetically favorable OTA surface coverage is equal to
 225 1.78%, exhibiting the lowest energy. The adsorption energy at this coverage is -6.627 eV per adsorbed
 226 ochratoxin molecule. The adsorption energy per each molecule for low concentration decreases
 227 monotonically with increasing percentage of coverage. This phenomenon could be attributed to the
 228 stabilization of the long-range interactions between the adsorbed OTA molecules³². The well-known
 229 fact is that the significantly different energies are associated with various conformation of the organic
 230 molecules³³. Once the percental surface coverage exceeds the limiting value, the distance between
 231 molecules is as low as the cross-linking and bond breaking processes starts to occur⁹. The initialization
 232 of the breakdown leads to the massive surface recombination which is associated with the desorption of
 233 OTA molecules. Such a process is indicated by the rapid increase of the adsorption energy. The
 234 competitive influence of mentioned processes will push the system to preserve the OTA concentration
 235 at the level close to optimal energetically stable.

236

237 3.2. *Ab-initio* Simulations of ND-OTA Complex

238 The diamond slab containing single OTA molecule was utilized to simulate *ab-initio* band structure of
 239 the studied ND-OTA complex by means of DFT. The horizontal size of the slab was aligned to set the
 240 OTA coverage to 1.78%. The coverage of COOH was kept at 6.66%. The slab is displayed in **Figure**
 241 **3a**. Additionally, the reference, H-terminated diamond slab, covered only by COOH (see **Figure 3c**),
 242 has been created. **Figures 3b,d** display projected band structure based on the *ab-initio* simulations. This

243 type of the band structure includes the projection of a state on a specific group of atoms, in this case
244 OTA and COOH.



245
246 **Figure 3.** a) The model of diamond [111] surfaces with adsorbed ochratoxin; b) Projected band structure
247 of the ND-OTA complex; c) Reference model of the slab terminated by the mixture of COOH and H;
248 d) Projected band structure of the slab presented in c, red states were introduced by adsorbed molecules.
249 (Attn. The blue states were introduced by OTA, red by COOH, orange dashed lines indicate position of
250 states of NV⁻ defects as calculated previously³⁴ while black states are associated with the diamond slab).

251 In this work, the interaction of the adsorbed OTA molecules with NV⁻ color centers is particularly
252 investigated. The energy states of NV⁻ center were extensively studied up to now^{34–37}. Here, the available
253 literature data^{34–37} has been applied instead of calculating the position of the NV states. The band gap
254 of diamond as shown in **Figures 3b,d** (orange dashed lines).

255 The presented projected band structure data clearly shows that adsorption of both COOH and OTA
256 introduces the electron states in the band gap of the diamond. In the case of COOH functionalization
257 new energy band is introduced below the lower conduction band. As an effect, the band gap shrinks by
258 the 40% relative to the hydrogen-terminated surface bandgap. A similar effect, however at higher
259 concentration of carboxyl, was predicted on the ground of ab-initio simulation of nanodiamond cluster
260 electronic properties³⁸. Introduction of the OTA functionalization results in further shrinking of the
261 fundamental band gap, divided both by introduction of OTA energy levels into fundamental band gap
262 of diamond and upshift of the valence band. As an effect of combined processes, the bandgap width
263 shrinks by 84% in comparison to the hydrogen-terminated [111] diamond surface.

264 The introduction of the surface states by the adsorbent species is well-known, but in these particular
265 conditions the most important is the location of these states in the energy-momentum space. The states
266 residues in the region close to the states introduced by the NV⁻ centers. The overlapping of surface
267 termination states is particularly evident in **Figure 3b**, which presents the band structure of [111]
268 diamond surfaces covered by both COOH and OTA. Several states are positioned within the NV⁻
269 bandgap, implying the strong interactions between ND-NV and OTA, which could even deactivate the
270 NV fluorescence^{34,39}.

271 To get qualitative measure of influence of OTA functionalization effect on the electronic properties, the
272 work function (WF) calculations were conducted. Both band structure and WF were simulated using
273 similar model as shown in **Figure 3**. The electron WF was calculated for different cases of surface
274 functionalization. The fully hydrogenated surface results in WF of 4.83 eV being in agreement with
275 prior experimental data^{40,41} for [111] diamond. The partially hydrogen-terminated diamond
276 functionalized with 6.66% of COOH groups (see **Figure 3c**) manifests WF equal to 6.21 eV. Finally,
277 the adsorption of 1.78% OTA results in WF of 6.49 eV (see **Figure 3a**). Observed changes are in
278 agreement with approach described in⁴² where WF values could be recalculated to the electron affinities.

279 The hydrogen termination induces the formation of the positively-charged surface, causing band
280 bending close to the diamond surface⁴³, thus NV centers will be favored to convert in the neutrally
281 charged state. According to conducted DFT simulation, OTA-coated diamond [111] surface will exhibit
282 positive electron affinity. This suggests that the surface will be negatively-charged.

283 Despite the relatively low concentrations of both COOH and OTA, the band structure of the ND-OTA
284 complex was significantly distorted by the covalent adsorption of OTA. Qualitative analysis of the
285 projected band structure and quantitative studies on the chemical potentials lead to the conclusion that
286 binding of OTA to the nanodiamond surface should stabilize concentrations of the NV⁻ centers.

287 Spectroscopic experiments revealed the decay in the fluorescence emission of the ND-OTA complexes
288 in function of increased the ct DNA concentrations (**Figure 6**). The simulation results suggest that the
289 light scattering and absorption or fluorescence quenching in the DNA-rich buffer are additional
290 processes responsible for the observed decay effect.

291

292

293

294

295

296



297

298 *3.3. Spectroscopic studies on the ND-OTA interactions with DNA*

299 Phosphate chromophores and aromatic bases are the cause of the characteristic DNA absorption peak
300 positioned at *ca.* 260 nm. The chromophore groups, namely purines—adenine and guanine—and
301 pyrimidines—cytosine and thymine, are the cause of the given maximum absorption peak ⁴⁴. Thanks to
302 this characteristic, one can utilize UV-Vis absorption measurement for the detection of various complex
303 formations. This technique, taking into account its simplicity and effectiveness, enables the detection of
304 various DNA–molecule interactions and the formation of new complexes. As the result of these spatial
305 changes, the absorbance intensity in the UV-Vis range as well as the band position are altered.
306 Bathochromism is observed during intercalation if the π^* orbital of the intercalating molecule couples
307 with the π orbital of the DNA base pairs, resulting in the decreased π^* transition energy. However, the
308 coupling π orbital is not fully saturated with electrons. To detect an interaction between DNA and a
309 chosen molecule, one can observe the shift in the maximum position of this band before and after the
310 addition of the ligand to the tested DNA solution.

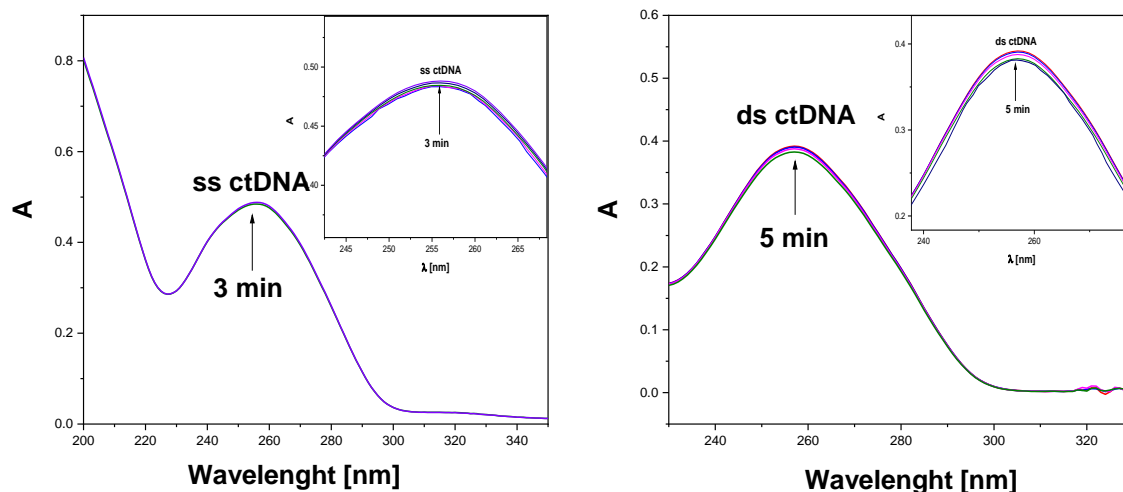
311 UV–Vis is usually used as a standard technique to quantify the amount of DNA in a sample. DNA bases
312 absorb strongly at 260 nm in an aqueous buffered solution at pH 7.4 ⁶. The absorbance values obtained
313 for this wavelength are used for the calculation of the DNA concentration and the stability analysis.
314 OTA was dissolved in PBS, pH 7.4. In the present experiments, the addition of 10 μ L of calf thymus
315 DNA (ct DNA) to OTA strongly influenced the UV spectra. The absorption band intensity regularly
316 decreased over time, which was also observed in many other studies ^{45,46}. Usually, the time needed to
317 establish the reaction equilibria was around 3–5 min ⁴⁷. In the present study, the overall time for the
318 determination of equilibria was 3 min for ss ct DNA and 5 min for ds ct DNA (**Figure 4**). This time was
319 accepted as optimal for the intercalation, to study the effects of OTA interactions with ct DNA ⁴⁶.

320

321

322





323
 324 **Figure 4.** The influence of the incubation time on the band intensity of OTA (2×10^{-4} M) after addition of ct DNA,
 325 10 μ L (ss ct DNA and ds ct DNA) in aqueous phosphate buffer solution, pH 7.4.

326 The UV spectra of the ND-OTA suspensions with different concentrations of ct DNA were obtained.
 327 As shown in **Figure 5**, with increasing concentrations of ct DNA, the intrinsic binding constant K_b of
 328 OTA with ct DNA can be determined according to Benesi–Hildebrand equation:

$$329 \quad \frac{A_0}{A - A_0} = \frac{\varepsilon_G}{\varepsilon_{H-G} - \varepsilon_G} + \frac{\varepsilon_G}{\varepsilon_{H-G} - \varepsilon_G} \times \frac{1}{K_b [DNA]}$$

330
 331 where K_b is the binding constant, A_0 and A are the absorbance of the OTA and its complex with ct DNA,
 332 and ε_{H-G} are the absorption coefficients of the OTA

333 **Figure 5** shows the absorption spectra of OTA in the presence of the increasing amounts of ct DNA to
 334 decrease in the peak intensities. Intercalating binding commonly results in the hypochromic and
 335 bathochromic effect of the intercalated chromophore transition. The spectral changes observed in the
 336 form of ‘hypochromism’ effect during the process, reflect the change in conformation of DNA and
 337 structure of DNA. It has been reported in literature that hypochromism is due to the intercalative mode
 338 involving a strong stacking interaction between an aromatic chromophore of a molecules and base pairs
 339 of DNA. Generally, the external groove binding causes a slight spectral shift, a hyperchromic effect. In
 340 all the spectra obtained, we observed the band with the maximum absorption in 270 nm, but for 10%
 341 spirit vinegar we observed the maximum at 230 nm.

342 Furthermore, comparing with the K_b value of other DNA groove mycotoxin binders, the binding mode
 343 between OTA and the ct DNA was deduced as groove binding. The association constant can be obtained
 344 from the intercept-to-slope ratios of $A_0/(A - A_0)$ vs. $1/[DNA]$ plots. Based on the intersection-to-slope
 345 ratio, the greatest K_b value was calculated as $3.27 \times 10^5 \text{ M}^{-1}$ for the diamond suspended in the green tea

346 solution. The K_b binding constant values reported herein are higher than those typically found for the
347 well-known toxins (**Table 2**) such as Aflatoxin B1 ($K_b = 7.60 \times 10^4 \text{ M}^{-1}$) and Wortmannin ($K_b = 2.20 \times 10^4$
348 M^{-1}).

349

350 **Table 2.** Comparison of the binding parameters for various toxins–ct DNA interactions obtained using UV-Vis
351 spectroscopy.

Compound	Binding constant [M^{-1}]	References
Isoxazolcurcumin	1.15×10^4	45
Wortmannin	2.20×10^4	48
Farrerol	11.80×10^5	49
Aflatoxin B1	7.60×10^4	50

352

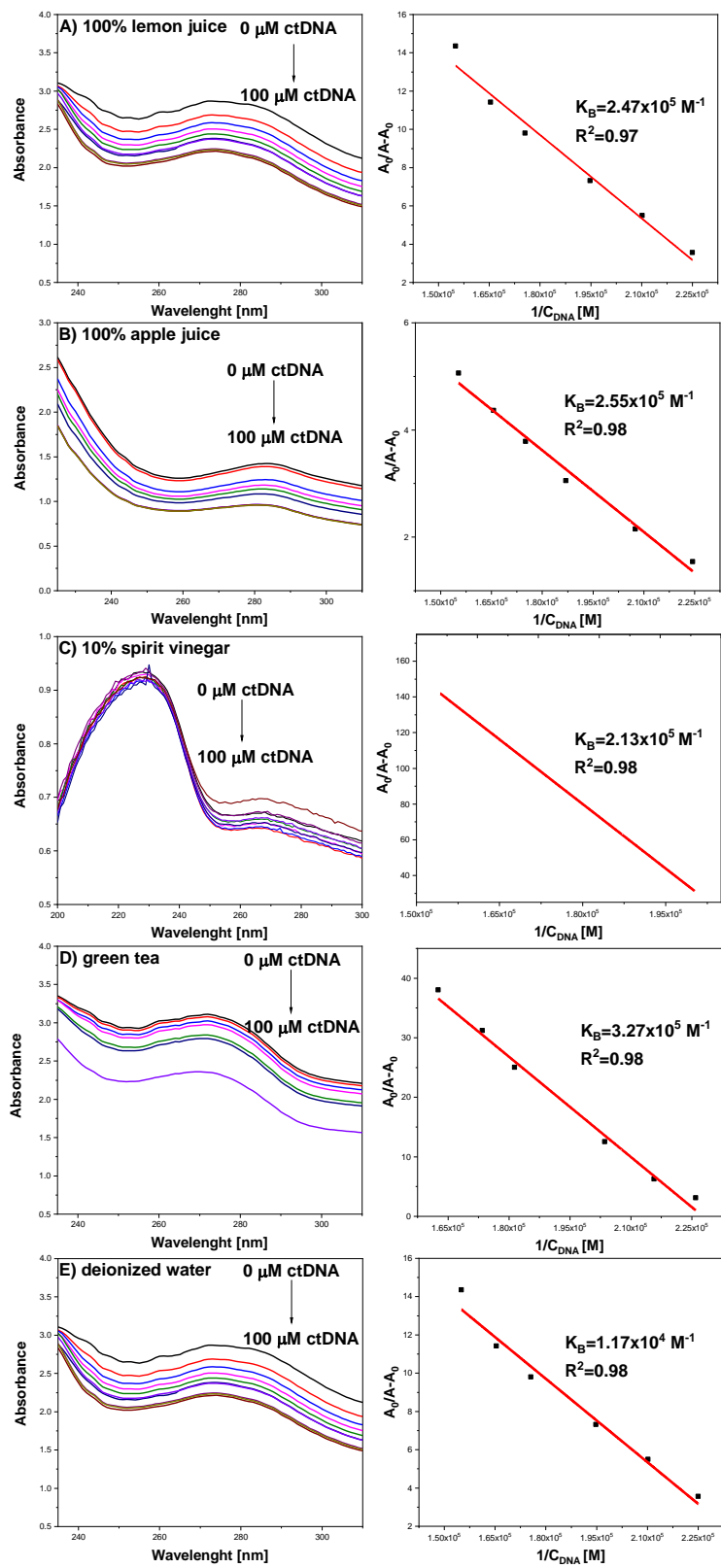
353

354

355

356





357

358 **Figure 5.** UV-Vis absorption spectra of OTA in different comestible liquids and plots of $(A_0/(A-A_0))$

359 versus $1/[DNA]$.



360

361 3.4. Fluorescent Analysis of the ND-OTA complex with DNA

362 The fluorescence spectra were obtained for the whole suspension (solvent, diamonds, OTA, ct DNA)
363 and were dominated by the fluorescence of diamonds which emit such intense radiation due to the
364 nitrogen-vacancy (NV) fluorescent color centers contained therein (**Figure 6**). The fluorescence
365 intensities decreased regularly with the increase of ct DNA concentration. The titration data were
366 analyzed according to the Stern–Volmer equation and investigated on the interaction types of ct DNA
367 with the five suspensions of the nanodiamonds. The fluorescent intensity significantly decreased with
368 increasing concentration of ct DNA. Therefore, fluorescence data could be studied using the Stern–
369 Volmer equation ⁵¹:

$$370 \quad \frac{F_0}{F_0 - F} = \frac{1}{f_a K_{SV}} \frac{1}{[ct DNA]} + \frac{1}{f_a}$$

371 where F_0 and F are the fluorescence intensities in the absence and presence of a quencher; f_a is the
372 fraction of the accessible fluorescence; K_{SV} is the quenching rate constant of the biomolecules, and $[ct$
373 DNA] is a concentration of calf thymus DNA.

374 To elaborate on the fluorescence exhibited by the nanodiamonds containing the NV centers, it is
375 advisable to concentrate first on the analysis of the spectra registered for the reference suspension based
376 on deionized water. This suspension was selected as it is least likely to alter the signal emitted by the
377 particles. Local maxima at 575 nm and 637 nm are the zero–phonon lines (ZPLs) of NV^0 and NV^-
378 centers, respectively ⁵². The much higher intensity of the ZPL of the negatively–charged centers
379 indicates their quantitative advantage over their electrically neutral counterparts. While the ZPL of NV^-
380 centers is clearly visible in every fluorescence spectrum registered in the experiment, the ZPL of NV^0
381 centers is quenched by the liquid medium in the suspensions based on lemon juice, apple juice, and
382 green tea. Broad peaks at 659 nm and 682 nm are the vibronic (phonon) sidebands of the NV^- centers ⁵³
383 with the known energy shifts of 65 meV ⁵⁴ and 63 meV ⁵², respectively. It is worth noting that the
384 majority of the signal emitted by the NV^- centers falls to the phonon sidebands, and not the ZPL, which
385 is a common occurrence when the measurements are carried out at room temperature ⁵⁵.

386 In every fluorescence spectrum of the sample based on the lemon juice there is a very intensive, broad
387 peak observed at 677 nm. This peak is a superposition of the 2nd phonon sideband of the NV^- centers,
388 and the maximum already present in the signal emitted by the pure lemon juice. A broad peak at 585 nm
389 registered for the suspensions based on the green tea comes from the dispersion medium itself. The same
390 peak has been identified in the spectrum of pure green tea. Lin *et al.* ⁵⁶ found that the emission intensity
391 in the range of 500–600 nm varies significantly between various kinds of green tea.



392 The OTA–DNA binding mode can be determined by fluorescence spectroscopy and various analytical
393 tools based on the fluorescence emission can also provide particularly useful information. Moreover,
394 the effective interaction with DNA usually causes a significant change of the fluorescence intensity as
395 a consequence of various factors. Representative spectra obtained for OTA in the absence and the
396 presence of calf thymus DNA dissolved in the solution are shown in **Figure 6**. We observed that with
397 the increasing DNA concentration, the emission spectra of OTA show remarkable distribution and
398 hyperchromic effect.

399 Given that OTA could emit fluorescence under ultraviolet irradiation, a series of experiments based on
400 the fluorescence spectroscopy were performed to explore the binding mechanism of mycotoxin to ct
401 DNA. The fluorescence intensity of OTA–DNA complex is quenched upon the addition of ct DNA.
402 OTA on the nanodiamond surface in lemon juice displayed strong emission spectra, with emission local
403 maximum at 637 nm. After the addition of ct DNA in a small concentration to OTA solution, we
404 observed that the position and shape of the peaks did not change. Thus, it can be assumed that OTA
405 interacts with ds ct DNA through noncovalent bonds rather than covalent bonds⁵⁷. The K_{SV} value of the
406 OTA–DNA complex at 298 K in various nanodiamond suspensions is presented in **Table 3**. The highest
407 value K_{sv} of the OTA–DNA complex was $8.12 \times 10^5 \text{ M}^{-1}$ on surfaces of nanodiamonds suspended in
408 green tea. A comparison shows that the K_{sv} of the OTA–DNA complex on nanodiamonds using green
409 tea solution was greater than in the case of other solutions. The difference in K_{sv} depends mainly on the
410 structural differences of the solution. Green tea contains other compounds less analeptic than caffeine,
411 xanthine derivatives, including theobromine, theanine, and theophylline which belong to the group of
412 polyphenols^{58,59}. This effect indicates that the hexatomic ring of OTA immobilized on nanodiamond
413 suspended in green tea has a larger dimension and stronger stability than the other nanodiamonds,
414 resulting in a stronger DNA binding.

415



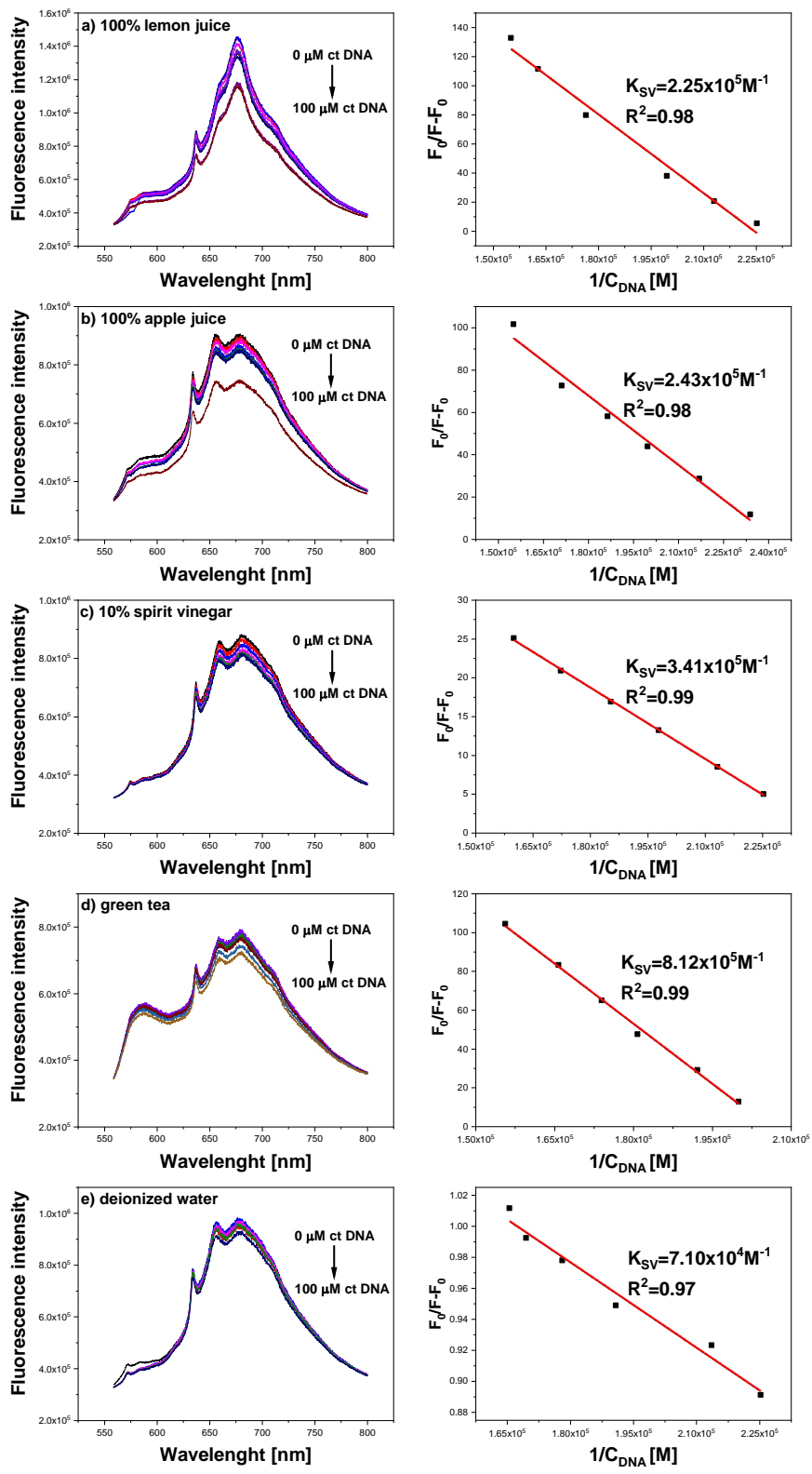
416 **Table 3.** Binding constants for OTA–ct DNA interaction.

Nanodiamond suspensions	Binding constant K_{sv} [M^{-1}]
Lemon juice	2.25×10^5
Apple juice	2.43×10^5
Deionized water	7.10×10^4
Green tea	8.12×10^5
Vinegar	3.41×10^5

417

418

419



420

421

422

423

Figure 6. Fluorescence emission spectra of OTA–DNA system in various comestible liquids and plots of $(F/(F_0-F))$ versus $1/[DNA]$.

424

425

426 *3.5. Analysis of the Particles Electric Potential*

427 Zeta potential measurements were conducted to investigate the variation of the surface charge at each
428 experimental step (**Figure 7a**). The carboxylated NDs, OTA-coated NDs, and OTA-coated NDs in the
429 presence of the DNA in the sample have been investigated in comestible liquids, namely vinegar, lemon
430 juice, apple juice, green tea, and deionized water. **Table 1** presents the pH values of the utilized liquids.

431 First, we measured the zeta potential of carboxylated NDs. At low pH values (lemon juice, apple juice,
432 and vinegar) the zeta potential oscillates around 0 mV, reaching a minimum value of ~ -5 mV for the
433 apple juice. This behavior is attributed to a large amount of mobile H⁺ ions present in these suspensions,
434 making the oxidized NDs' surfaces electroneutral, thus, unstable and prone to aggregation.

435 With the increase in pH, the zeta potential is decreasing, reaching the values of -20 and -43 mV for the
436 green tea and water, respectively. Once the pH increases, H⁺ ions become depleted from the solution as
437 well as from the carboxyl groups present on the NDs' surfaces, generating the negatively charged
438 particles and, therefore, stabilizing them in the solutions ⁶⁰.

439 Next, OTA-coated NDs were measured. OTA contains phenolic and carboxylic groups (**Figure 9**), and
440 therefore can exist in different ionization states: carboxy ionized (COO⁻), phenolic ionized (ArO⁻),
441 dianionic form (both carboxylic and phenolic ionized), depending on the local pH. The reported pKa
442 values of the carboxyl group and the phenolic group of OTA are in the range of 4.2–4.4 and 7.0–7.3,
443 respectively ⁶¹. Furthermore, knowing that the OTA's carboxyl group is involved in the covalent surface
444 functionalization, the only part which can be ionized is the phenolic group. For this reason, ND-OTA
445 complexes in acidic environments stay electroneutral and prone to aggregation as OTA exists in this
446 condition in a neutral state.

447 However, in the case of water and green tea, considering their pH, both forms of OTA are simultaneously
448 present in various ratios in these solutions (neutral and anionic form). Thus, for instance, in the case of
449 water, we observed slight neutralization of the negative charge and an increase in zeta potential from -43
450 to -38 mV. In the case of green tea, we did not observe any changes, which can be caused by the
451 involvement of two forms of OTA on the ND surface. Consequently, the final effect may be an average
452 of these two. Another reason may be the influence of the co-existing green tea ingredients. Green tea
453 contains as many as 200 bioactive compounds, such as polyphenols, caffeine, theanine, which also can
454 neutralize OTA influence.

455 The last and the most complicated case was OTA-coated ND in the presence of ct DNA. There are many
456 factors involved in the interaction of a compound with DNA, such as temperature, ionic strength, or



457 temperature. The picture is even more complicated if the compound—in our work OTA—exists in more
458 than one form in the solution, as each form interacts with DNA differently. In general, DNA is a negative
459 polymer, hence this molecule exhibits higher interactions with cationic species than the neutral species.
460 On the other hand, these interactions are greater than in case of species that are negatively charged.

461 Zeta potential measurements in acidic liquids revealed no observable changes, although a neutral form
462 of the OTA may bind the DNA. However, DNA can change its 3D structure in highly acidic
463 environments, starting from an elongated coil state to a compact one, what is closely related to its charge
464 neutralization⁶². Also, DNA may partially denature in such an extreme condition, as a result making the
465 interaction of DNA with OTA impossible in both cases.

466 In the case of water, as mentioned before, neutral and anionic form of OTA are present on its surface,
467 while DNA will exist in an elongated structure with a negative charge. Therefore, the interaction
468 between OTA and DNA may be somehow impeded. However, as reported by Saha *et al.*⁶³, the presence
469 of the DNA in the examined sample can change the pKa value of the binding compound, in our case
470 OTA immobilized on NDs' surface⁶³ and thereby changing the zeta potential of the surface. Another
471 reason for the increase of the zeta potential value from -38 to -34 mV is the interaction (groove binding,
472 or intercalation) of OTA with DNA, thus, neutralizing the negative charge of added DNA, as well as
473 anionic phenolic group of OTA.

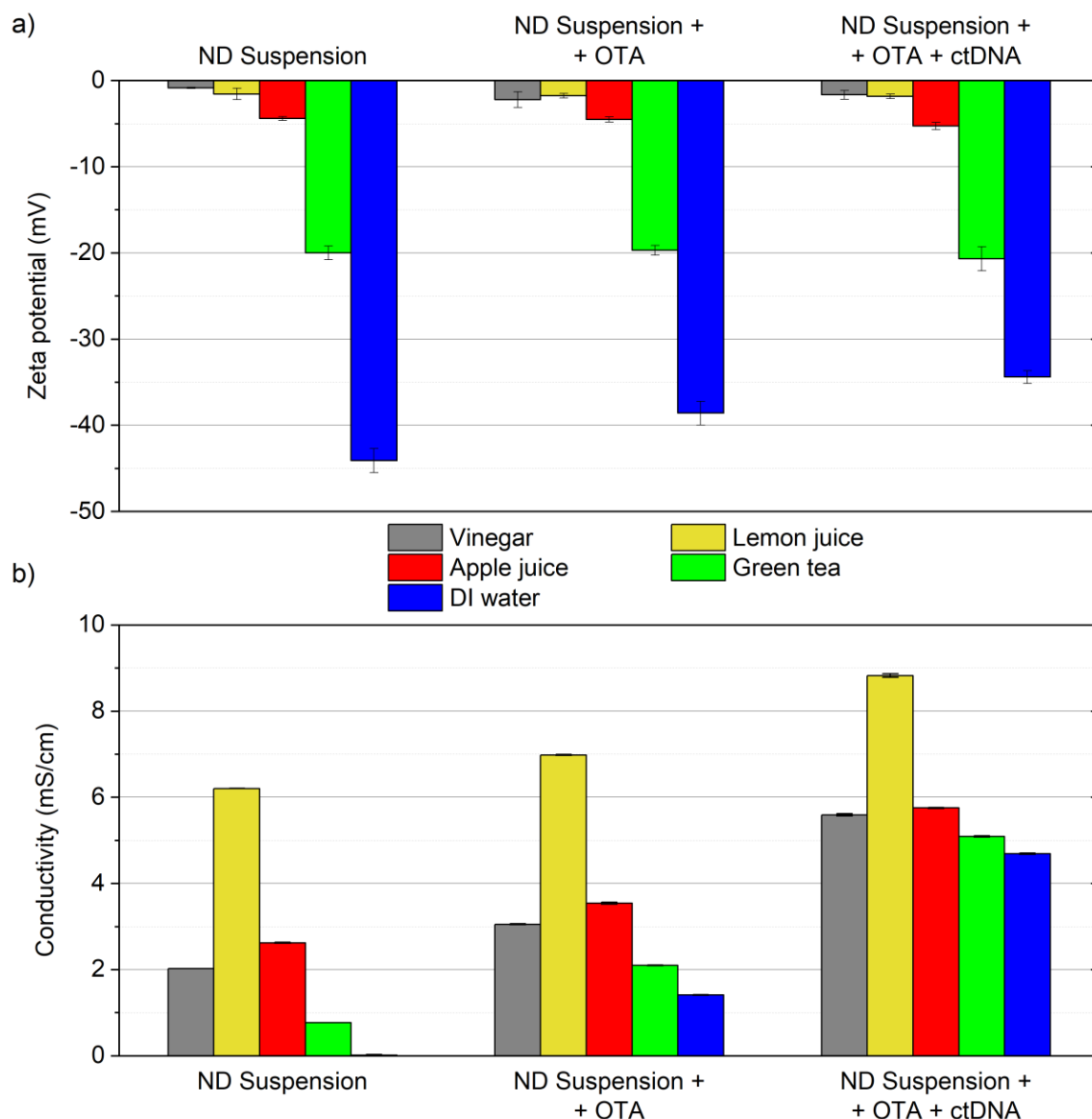
474 In the case of green tea, again, we did not observe any noticeable changes in the zeta potential. This
475 effect can be justified by the same arguments as previously. In water, both forms of OTA are present;
476 the pKa value of OTA can vary because of the DNA presence; interaction of OTA with DNA also may
477 take place, however, the net charge may be neutralized by co-existing green tea ingredients.

478 The conductivities of the nanodiamond suspensions at different stages of the particles modification are
479 presented in **Figure 7b**. The deionized water is the only dispersion medium that exhibits virtually no
480 electrical conductivity with suspended unmodified nanodiamonds. At the same stage, every other
481 sample shows initial conductivity, with the suspension based on the lemon juice revealing the highest
482 value, followed by the sample based on the apple juice, then on the vinegar, and finally on the green tea.
483 This relation among the conductivities of the suspensions is preserved at every stage of the modification
484 of the nanodiamonds. The attachment of the OTA to the surfaces of the diamond particles, as well as
485 the addition of double-stranded ct DNA to the suspensions, increase the overall conductivities of the
486 samples.

487

488





489

490 **Figure 7.** The electrical properties of the nanodiamond suspensions based on the comestible liquids;
 491 “ND Suspension” – the suspensions of unmodified nanodiamonds (0.1% concentration); “ND
 492 Suspension + OTA” – the suspensions of the nanodiamonds with OTA attached to the surfaces of the
 493 particles; “ND Suspension + OTA + ct DNA” – mixtures containing 2 mL of the nanodiamond
 494 suspensions with OTA attached to the surfaces of the particles and 0.5 mL of the solvent containing ds
 495 ct DNA; a) zeta potential; b) conductivity.

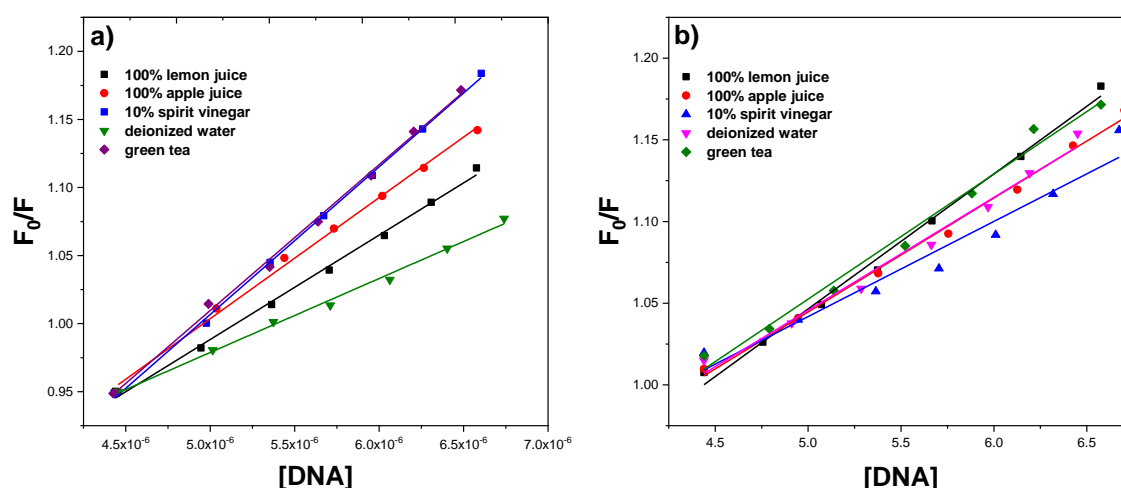
496

497 3.6. Effects of Mycotoxins on the Characteristics of the Denatured DNA

498 A difference was observed in the quenching effect of single-stranded DNA (ssDNA) and
 499 double-stranded DNA (dsDNA) when molecules were bound to DNA based on different interaction
 500 modes. In the groove bounding mode, the quenching interactions of dsDNA should be stronger than for

501 ssDNA. Weaker quenching effects of dsDNA comparing with ssDNA also slightly differed if small
 502 molecules intercalated between the DNA base pairs. The double strands were denatured. The quenching
 503 effects of both ssDNA and dsDNA also slightly differed if small molecules interacted with the
 504 phosphates groups of DNA based on electrostatic interactions⁶⁴⁻⁶⁶. The fluorescence quenching plots of
 505 OTA upon the addition of different concentrations of dsDNA and ssDNA are shown in **Figure 8**. The
 506 dsDNA exhibited a greater slope than ssDNA in OTA.

507



508

509 **Figure 8.** Fluorescence quenching plots of OTA for a) single-stranded DNA (ssDNA) and b) double-
 510 stranded DNA (dsDNA) in different comestible liquids in, $C_{OTA} = 2 \times 10^{-3} M$. F_0 is the fluorescence
 511 intensity of OTA and F is the fluorescence intensity of OTA for the various ssDNA and dsDNA
 512 concentrations.

513

514 Conclusions

515 In summary, the interactions of ND-OTA complexes with ct DNA were investigated using spectroscopic
 516 methods applying nitrogen-vacancy rich nanodiamonds suspensions. The characteristics of the
 517 interaction between OTA and ct DNA were studied in different comestible liquids. The fluorescent
 518 measurements demonstrated that the intensity of the fluorescence significantly decreased with the
 519 increasing concentration of ct DNA. The UV-Vis studies indicated that the increasing concentrations of
 520 ct DNA lead to a decrease in the peak intensities.

521 We obtained the binding constants and the binding site sizes (0.97) of OTA with ct DNA at room
 522 temperature. Moreover, we managed to form a complex with ct DNA where a part of OTA occupies a
 523 space within the groove binding and the rest slips in between the stacked base pairs of duplex DNA via
 524 the intercalation mode of binding.

525 The presence of the adsorbed species introduces additional states to the fundamental diamond bandgap.
526 The energy states of NV⁻ center lies near the states introduced by the adsorbed ochratoxin. Importantly,
527 the states introduced by OTA lie in the bandgap of NV⁻ center lowering its width and changing the
528 optical absorption and emission spectrum of the center.

529 The present study provides detailed information on the binding affinity, the mode of binding interaction,
530 the main forces of OTA–ct DNA interactions, and the structure of OTA–DNA complex, which enables
531 the further elucidation of the DNA degradation mechanism.

532

533 **Acknowledgments**

534 This work was supported by the TEAM-NET program of the Foundation for Polish Science co-financed
535 by the European Union under the European Regional Development Fund QUNNA POIR.04.04.00-00-
536 1644 /18.

537

538 **Bibliography:**

- 539 (1) Zheng, M. Z.; Richard, J. L.; Binder, J. A Review of Rapid Methods for the Analysis of Mycotoxins.
540 *Mycopathologia* **2006**, *161* (5), 261–273. <https://doi.org/10.1007/s11046-006-0215-6>.
- 541 (2) Calado, T.; Fernández-Cruz, M. L.; Cabo Verde, S.; Venâncio, A.; Abrunhosa, L. Gamma
542 Irradiation Effects on Ochratoxin A: Degradation, Cytotoxicity and Application in Food. *Food*
543 *Chemistry* **2018**, *240*, 463–471. <https://doi.org/10.1016/j.foodchem.2017.07.136>.
- 544 (3) Mally, A.; Zepnik, H.; Wanek, P.; Eder, E.; Dingley, K.; Ihmels, H.; Völkel, W.; Dekant, W.
545 Ochratoxin A: Lack of Formation of Covalent DNA Adducts. *Chemical research in toxicology*
546 **2004**, *17*, 234–242. <https://doi.org/10.1021/tx034188m>.
- 547 (4) Kou, S.-B.; Lou, Y.-Y.; Zhou, K.-L.; Wang, B.-L.; Lin, Z.-Y.; Shi, J.-H. In Vitro Exploration of
548 Interaction Behavior between Calf Thymus DNA and Fenhexamid with the Help of Multi-
549 Spectroscopic Methods and Molecular Dynamics Simulations. *Journal of Molecular Liquids*
550 **2019**, *296*, 112067. <https://doi.org/10.1016/j.molliq.2019.112067>.
- 551 (5) Shi, J.-H.; Zhou, K.-L.; Lou, Y.-Y.; Pan, D.-Q. Multi-Spectroscopic and Molecular Docking Studies
552 on the Interaction of Darunavir, a HIV Protease Inhibitor with Calf Thymus DNA. *Spectrochimica*
553 *Acta Part A: Molecular and Biomolecular Spectroscopy* **2018**, *193*, 14–22.
554 <https://doi.org/10.1016/j.saa.2017.11.061>.
- 555 (6) Biało-brzeska, W.; Niedziałkowski, P.; Malinowska, N.; Cebula, Z.; Ossowski, T. Analysis of
556 Interactions between Calf Thymus DNA and 1,5-Di(Piperazin-1-Yl)Anthracene-9,10-Dione Using
557 Spectroscopic and Electrochemical Methods. *Journal of Molecular Liquids* **2019**, *289*, 111080.
558 <https://doi.org/10.1016/j.molliq.2019.111080>.
- 559 (7) da Silva, C. M.; Silva, M. M.; Reis, F. S.; Ruiz, A. L. T. G.; de Carvalho, J. E.; Santos, J. C. C.;
560 Figueiredo, I. M.; Alves, R. B.; Modolo, L. V.; de Fátima, Â. Studies on Free Radical Scavenging,
561 Cancer Cell Antiproliferation, and Calf Thymus DNA Interaction of Schiff Bases. *Journal of*
562 *Photochemistry and Photobiology B: Biology* **2017**, *172*, 129–138.
563 <https://doi.org/10.1016/j.jphotobiol.2017.05.020>.
- 564 (8) Rovina, K.; Shaera, S. N.; Vonnice, J. M.; Yi, S. X. Recent Biosensors Technologies for Detection
565 of Mycotoxin in Food Products. *Mycotoxins and Food Safety* **2019**.
566 <https://doi.org/10.5772/intechopen.89022>.

- 567 (9) Tian, Y.; Larsson, K. Process of Diamond Surface Termination by Carboxylic and Amino Groups:
568 A Quantum Mechanics Approach. *Journal of Material Science & Engineering* **2019**, *08* (01), 1–
569 10. <https://doi.org/10.4172/2169-0022.1000506>.
- 570 (10) Chauhan, S.; Jain, N.; Nagaich, U. Nanodiamonds with Powerful Ability for Drug Delivery and
571 Biomedical Applications: Recent Updates on in Vivo Study and Patents. *Journal of*
572 *Pharmaceutical Analysis* **2020**, *10* (1), 1–12. <https://doi.org/10.1016/j.jpha.2019.09.003>.
- 573 (11) Kaur, R.; Badea, I. Nanodiamonds as Novel Nanomaterials for Biomedical Applications: Drug
574 Delivery and Imaging Systems. *Int J Nanomedicine* **2013**, *8*, 203–220.
575 <https://doi.org/10.2147/IJN.S37348>.
- 576 (12) Acosta, V.; Hemmer, P. Nitrogen-Vacancy Centers: Physics and Applications. *MRS Bulletin* **2013**,
577 *38* (2), 127–130. <https://doi.org/10.1557/mrs.2013.18>.
- 578 (13) Sękowska, A.; Majchrowicz, D.; Sabisz, A.; Ficek, M.; Bułto-Piontecka, B.; Kosowska, M.; Jing, L.;
579 Bogdanowicz, R.; Szczerska, M. Nanodiamond Phantoms Mimicking Human Liver: Perspective
580 to Calibration of T1 Relaxation Time in Magnetic Resonance Imaging. *Scientific Reports* **2020**, *10*
581 (1), 6446. <https://doi.org/10.1038/s41598-020-63581-9>.
- 582 (14) Wojciechowski, A. M.; Nakonieczna, P.; Mrózek, M.; Sycz, K.; Kruk, A.; Ficek, M.; Głowacki, M.;
583 Bogdanowicz, R.; Gawlik, W. Optical Magnetometry Based on Nanodiamonds with Nitrogen-
584 Vacancy Color Centers. *Materials* **2019**, *12* (18), 2951. <https://doi.org/10.3390/ma12182951>.
- 585 (15) Jelezko, F.; Wrachtrup, J. Single Defect Centres in Diamond: A Review. *physica status solidi (a)*
586 **2006**, *203* (13), 3207–3225. <https://doi.org/10.1002/pssa.200671403>.
- 587 (16) Bourgeois, E.; Gulka, M.; Nesladek, M. Photoelectric Detection and Quantum Readout of
588 Nitrogen-Vacancy Center Spin States in Diamond. *Advanced Optical Materials* **2020**, *8* (12),
589 1902132. <https://doi.org/10.1002/adom.201902132>.
- 590 (17) Fu, C.-C.; Lee, H.-Y.; Chen, K.; Lim, T.-S.; Wu, H.-Y.; Lin, P.-K.; Wei, P.-K.; Tsao, P.-H.; Chang, H.-C.;
591 Fann, W. Characterization and Application of Single Fluorescent Nanodiamonds as Cellular
592 Biomarkers. *PNAS* **2007**, *104* (3), 727–732. <https://doi.org/10.1073/pnas.0605409104>.
- 593 (18) Barone, F. C.; Marcinkiewicz, C.; Li, J.; Feng, Y.; Sternberg, M.; Lelkes, P. I.; Rosenbaum-Halevi,
594 D.; Gerstenhaber, J. A.; Feuerstein, G. Z. Long-Term Biocompatibility of Fluorescent Diamonds-
595 (NV)-Z~800 Nm in Rats: Survival, Morbidity, Histopathology, Particle Distribution and Excretion
596 Studies (Part IV). *Int J Nanomedicine* **2019**, *14*, 1163–1175.
597 <https://doi.org/10.2147/IJN.S189048>.
- 598 (19) McDonald, M.; Monaco, A.; Vahidpour, F.; Haenen, K.; Giugliano, M.; Nesladek, M. Diamond
599 Microelectrode Arrays for in Vitro Neuronal Recordings. *MRS Communications* **2017**, *7* (3), 683–
600 690. <https://doi.org/10.1557/mrc.2017.62>.
- 601 (20) Wąsowicz, M.; Ficek, M.; Wróbel, M. S.; Chakraborty, R.; Fixler, D.; Wierzba, P.; Jędrzejewska-
602 Szczerska, M. Haemocompatibility of Modified Nanodiamonds. *Materials* **2017**, *10* (4), 352.
603 <https://doi.org/10.3390/ma10040352>.
- 604 (21) Schirhagl, R.; Chang, K.; Loretz, M.; Degen, C. L. Nitrogen-Vacancy Centers in Diamond:
605 Nanoscale Sensors for Physics and Biology. *Annual Review of Physical Chemistry* **2014**, *65* (1),
606 83–105. <https://doi.org/10.1146/annurev-physchem-040513-103659>.
- 607 (22) Kawai, S.; Yamano, H.; Sonoda, T.; Kato, K.; Buendia, J. J.; Kageura, T.; Fukuda, R.; Okada, T.;
608 Tanii, T.; Higuchi, T.; Haruyama, M.; Yamada, K.; Onoda, S.; Ohshima, T.; Kada, W.; Hanaizumi,
609 O.; Stacey, A.; Teraji, T.; Kono, S.; Isoya, J.; Kawarada, H. Nitrogen-Terminated Diamond Surface
610 for Nanoscale NMR by Shallow Nitrogen-Vacancy Centers. *J. Phys. Chem. C* **2019**, *123* (6), 3594–
611 3604. <https://doi.org/10.1021/acs.jpcc.8b11274>.
- 612 (23) Gibson, N. M.; Luo, T. J. M.; Brenner, D. W.; Shenderova, O. Immobilization of Mycotoxins on
613 Modified Nanodiamond Substrates. *Biointerphases* **2011**, *6* (4), 210–217.
614 <https://doi.org/10.1116/1.3672489>.
- 615 (24) Puzyr', A. P.; Burov, A. E.; Bondar', V. S.; Trusov, Yu. N. Neutralization of Aflatoxin B1 by Ozone
616 Treatment and Adsorption by Nanodiamonds. *Nanotechnol Russia* **2010**, *5* (1), 137–141.
617 <https://doi.org/10.1134/S1995078010010143>.
- 618 (25) Atomistix Toolkit Version 2019.03, Synopsys QuantumWise A/S (Www.Quantumwise.Com).

- 619 (26) Kim, S.; Chen, J.; Cheng, T.; Gindulyte, A.; He, J.; He, S.; Li, Q.; Shoemaker, B. A.; Thiessen, P. A.;
620 Yu, B.; Zaslavsky, L.; Zhang, J.; Bolton, E. E. PubChem 2019 Update: Improved Access to
621 Chemical Data. *Nucleic Acids Research* **2019**, *47* (D1), D1102–D1109.
622 <https://doi.org/10.1093/nar/gky1033>.
- 623 (27) Smidstrup, S.; Markussen, T.; Vancraeyveld, P.; Wellendorff, J.; Schneider, J.; Gunst, T.;
624 Verstichel, B.; Stradi, D.; Khomyakov, P. A.; Vej-Hansen, U. G.; Lee, M. E.; Chill, S. T.; Rasmussen,
625 F.; Penazzi, G.; Corsetti, F.; Ojanperä, A.; Jensen, K.; Palsgaard, M. L. N.; Martinez, U.; Blom, A.;
626 Brandbyge, M.; Stokbro, K. QuantumATK: An Integrated Platform of Electronic and Atomic-
627 Scale Modelling Tools. *Journal of Physics Condensed Matter* **2020**, *32* (1).
628 <https://doi.org/10.1088/1361-648X/ab4007>.
- 629 (28) Vashisth, A.; Ashraf, C.; Zhang, W.; Bakis, C. E.; Van Duin, A. C. T. Accelerated ReaxFF
630 Simulations for Describing the Reactive Cross-Linking of Polymers. *Journal of Physical Chemistry*
631 *A* **2018**, *122* (32), 6633–6642. <https://doi.org/10.1021/acs.jpca.8b03826>.
- 632 (29) Jos; Soler, M.; Emilio, A.; Julian, D. G.; Alberto, G.; Javier, J.; Pablo, O.; Daniel, S.; Nchez, P. The
633 SIESTA Method for Ab Initio Order-N Materials Simulation. *Journal of Physics: Condensed*
634 *Matter* **2002**, No. 11, 2745. <https://doi.org/10.1088/0953-8984/14/11/302>.
- 635 (30) van Setten, M. J.; Giantomassi, M.; Bousquet, E.; Verstraete, M. J.; Hamann, D. R.; Gonze, X.;
636 Rignanese, G. M. The PSEUDODOJO: Training and Grading a 85 Element Optimized Norm-
637 Conserving Pseudopotential Table. *Computer Physics Communications* **2018**, *226*, 39–54.
638 <https://doi.org/10.1016/j.cpc.2018.01.012>.
- 639 (31) Smidstrup, S.; Stradi, D.; Wellendorff, J.; Khomyakov, P. A.; Vej-Hansen, U. G.; Lee, M.-E.;
640 Ghosh, T.; Jónsson, E.; Jónsson, H.; Stokbro, K. First-Principles Green's-Function Method for
641 Surface Calculations: A Pseudopotential Localized Basis Set Approach. *Physical Review B* **2017**,
642 *96* (19), 195309. <https://doi.org/10.1103/PhysRevB.96.195309>.
- 643 (32) Knizhnik, A. A.; Polynskaya, Y. G.; Sinitisa, A. S.; Kuznetsov, N. M.; Belousov, S. I.; Chvalun, S. N.;
644 Potapkin, B. V. Analysis of Structural Organization and Interaction Mechanisms of Detonation
645 Nanodiamond Particles in Hydrosols. *Phys. Chem. Chem. Phys.* **2021**, *23* (1), 674–682.
646 <https://doi.org/10.1039/D0CP05533F>.
- 647 (33) Yeganeh, M.; Badieian Baghsiyahi, F. Exploring the Sensitivity of Nanodiamond to Sarafloxacin:
648 A DFT Approach. *Journal of Physics and Chemistry of Solids* **2019**, *124*, 235–241.
649 <https://doi.org/10.1016/j.jpcs.2018.09.032>.
- 650 (34) Chou, J.-P.; Gali, A. Nitrogen-Vacancy Diamond Sensor: Novel Diamond Surfaces from Ab Initio
651 Simulations. *MRS Communications* **2017**, *7* (3), 551–562. <https://doi.org/10.1557/mrc.2017.75>.
- 652 (35) Gali, A.; Fyta, M.; Kaxiras, E. Ab Initio Supercell Calculations on Nitrogen-Vacancy Center in
653 Diamond: Electronic Structure and Hyperfine Tensors. *Physical Review B - Condensed Matter*
654 *and Materials Physics* **2008**, *77* (15), 1–12. <https://doi.org/10.1103/PhysRevB.77.155206>.
- 655 (36) Kaviani, M.; Deák, P.; Aradi, B.; Frauenheim, T.; Chou, J. P.; Gali, A. Proper Surface Termination
656 for Luminescent Near-Surface NV Centers in Diamond. *Nano Letters* **2014**, *14* (8), 4772–4777.
657 <https://doi.org/10.1021/nl501927y>.
- 658 (37) Gali, Á. Ab Initio Theory of the Nitrogen-Vacancy Center in Diamond. *Nanophotonics* **2019**, *8*
659 (11), 1907–1943. <https://doi.org/10.1515/nanoph-2019-0154>.
- 660 (38) Brown, N.; Hod, O. Controlling the Electronic Properties of Nanodiamonds via Surface Chemical
661 Functionalization: A DFT Study. *J. Phys. Chem. C* **2014**, *118* (10), 5530–5537.
662 <https://doi.org/10.1021/jp409236t>.
- 663 (39) Makino, T.; Kato, H.; Shimizu, M.; Hatano, M.; Mizuochi, N. Charge State Control by Band
664 Engineering. In *Semiconductors and Semimetals*; Elsevier, 2020; Vol. 103, pp 137–159.
665 <https://doi.org/10.1016/bs.semsem.2020.03.005>.
- 666 (40) Cui, J. B.; Ristein, J.; Ley, L. Electron Affinity of the Bare and Hydrogen Covered Single Crystal
667 Diamond (111) Surface. *Phys. Rev. Lett.* **1998**, *81* (2), 429–432.
668 <https://doi.org/10.1103/PhysRevLett.81.429>.
- 669 (41) Mackie, W. A.; Plumlee, J. E.; Bell, A. E. Work Function Measurements of Diamond Film
670 Surfaces. *J. Vac. Sci. Technol. B* **1996**, *14* (3), 6.

- 671 (42) Maier, F.; Ristein, J.; Ley, L. Electron Affinity of Plasma-Hydrogenated and Chemically Oxidized
672 Diamond (100) Surfaces. *Phys. Rev. B* **2001**, *64* (16), 165411.
673 <https://doi.org/10.1103/PhysRevB.64.165411>.
- 674 (43) Laube, C.; Oeckinghaus, T.; Lehnert, J.; Griebel, J.; Knolle, W.; Denisenko, A.; Kahnt, A.; Meijer,
675 J.; Wrachtrup, J.; Abel, B. Controlling the Fluorescence Properties of Nitrogen Vacancy Centers
676 in Nanodiamonds. *Nanoscale* **2019**, *11* (4), 1770–1783. <https://doi.org/10.1039/C8NR07828A>.
- 677 (44) Skyrianou, K. C.; Psycharis, V.; Raptopoulou, C. P.; Kessissoglou, D. P.; Psomas, G. Nickel-
678 Quinolones Interaction. Part 4. Structure and Biological Evaluation of Nickel(II)-Enrofloxacin
679 Complexes Compared to Zinc(II) Analogues. *J. Inorg. Biochem.* **2011**, *105* (1), 63–74.
680 <https://doi.org/10.1016/j.jinorgbio.2010.09.007>.
- 681 (45) Bera, R.; Sahoo, B. K.; Ghosh, K. S.; Dasgupta, S. Studies on the Interaction of Isoxazolcurcumin
682 with Calf Thymus DNA. *International Journal of Biological Macromolecules* **2008**, *42* (1), 14–21.
683 <https://doi.org/10.1016/j.ijbiomac.2007.08.010>.
- 684 (46) Pakravan, P.; Masoudian, S. Study on the Interaction between Isatin- β -Thiosemicarbazone and
685 Calf Thymus DNA by Spectroscopic Techniques. *Iran J Pharm Res* **2015**, *14* (1), 111–123.
- 686 (47) Zhang, X.; Poniewierski, A.; Jelińska, A.; Zagożdżon, A.; Wisniewska, A.; Hou, S.; Hotyst, R.
687 Determination of Equilibrium and Rate Constants for Complex Formation by Fluorescence
688 Correlation Spectroscopy Supplemented by Dynamic Light Scattering and Taylor Dispersion
689 Analysis. *Soft Matter* **2016**, *12* (39), 8186–8194. <https://doi.org/10.1039/C6SM01791F>.
- 690 (48) Mehran, S.; Rasmi, Y.; Karamdel, H. R.; Hossinzadeh, R.; Gholinejad, Z. Study of the Binding
691 Interaction between Wortmannin and Calf Thymus DNA: Multispectroscopic and Molecular
692 Docking Studies <https://www.hindawi.com/journals/ecam/2019/4936351/> (accessed 2020 -09 -
693 02). <https://doi.org/10.1155/2019/4936351>.
- 694 (49) Zhang, G.; Fu, P.; Wang, L.; Hu, M. Molecular Spectroscopic Studies of Farrerol Interaction with
695 Calf Thymus DNA. *J. Agric. Food Chem.* **2011**, *59* (16), 8944–8952.
696 <https://doi.org/10.1021/jf2019006>.
- 697 (50) Ma, L.; Wang, J.; Zhang, Y. Probing the Characterization of the Interaction of Aflatoxins B1 and
698 G1 with Calf Thymus DNA In Vitro. *Toxins (Basel)* **2017**, *9* (7).
699 <https://doi.org/10.3390/toxins9070209>.
- 700 (51) Fluorescence Sensing. In *Principles of Fluorescence Spectroscopy*; Lakowicz, J. R., Ed.; Springer
701 US: Boston, MA, 2006; pp 623–673. https://doi.org/10.1007/978-0-387-46312-4_19.
- 702 (52) Su, Z.; Ren, Z.; Bao, Y.; Lao, X.; Zhang, J.; Zhang, J.; Zhu, D.; Lu, Y.; Hao, Y.; Xu, S. Luminescence
703 Landscapes of Nitrogen-Vacancy Centers in Diamond: Quasi-Localized Vibrational Resonances
704 and Selective Coupling. *J. Mater. Chem. C* **2019**, *7* (26), 8086–8091.
705 <https://doi.org/10.1039/C9TC01954E>.
- 706 (53) Chen, L.; Miao, X.; Ma, H.; Guo, L.; Wang, Z.; Yang, Z.; Fang, C.; Jia, X. Synthesis and
707 Characterization of Diamonds with Different Nitrogen Concentrations under High Pressure and
708 High Temperature Conditions. *CrystEngComm* **2018**, *20* (44), 7164–7169.
709 <https://doi.org/10.1039/C8CE01533C>.
- 710 (54) Yang, M.; Yuan, Q.; Gao, J.; Shu, S.; Chen, F.; Sun, H.; Nishimura, K.; Wang, S.; Yi, J.; Lin, C.-T.;
711 Jiang, N. A Diamond Temperature Sensor Based on the Energy Level Shift of Nitrogen-Vacancy
712 Color Centers. *Nanomaterials* **2019**, *9* (11), 1576. <https://doi.org/10.3390/nano9111576>.
- 713 (55) Bourgeois, E.; Gulka, M.; Nesladek, M. Photoelectric Detection and Quantum Readout of
714 Nitrogen-Vacancy Center Spin States in Diamond. *Advanced Optical Materials* **2020**, *8* (12),
715 1902132. <https://doi.org/10.1002/adom.201902132>.
- 716 (56) Lin, H.; Li, Z.; Lu, H.; Sun, S.; Chen, F.; Wei, K.; Ming, D. Robust Classification of Tea Based on
717 Multi-Channel LED-Induced Fluorescence and a Convolutional Neural Network. *Sensors* **2019**,
718 *19* (21), 4687. <https://doi.org/10.3390/s19214687>.
- 719 (57) Li, Y.; Zhang, G.; Tao, M. Binding Properties of Herbicide Chlorpropham to DNA: Spectroscopic,
720 Chemometrics and Modeling Investigations. *Journal of Photochemistry and Photobiology B:
721 Biology* **2014**, *138*, 109–117. <https://doi.org/10.1016/j.jphotobiol.2014.05.011>.



- 722 (58) Labieniec, M.; Gabryelak, T. Interactions of Tannic Acid and Its Derivatives (Ellagic and Gallic
723 Acid) with Calf Thymus DNA and Bovine Serum Albumin Using Spectroscopic Method. *J*
724 *Photochem Photobiol B* **2006**, *82* (1), 72–78. <https://doi.org/10.1016/j.jphotobiol.2005.09.005>.
- 725 (59) Nafisi, S.; Manouchehri, F.; Tajmir-Riahi, H.-A.; Varavipour, M. Structural Features of DNA
726 Interaction with Caffeine and Theophylline. *Journal of Molecular Structure* **2008**, *875* (1), 392–
727 399. <https://doi.org/10.1016/j.molstruc.2007.05.010>.
- 728 (60) Chakrapani, V.; Angus, J. C.; Anderson, A. B.; Wolter, S. D.; Stoner, B. R.; Sumanasekera, G. U.
729 Charge Transfer Equilibria Between Diamond and an Aqueous Oxygen Electrochemical Redox
730 Couple. *Science* **2007**, *318* (5855), 1424–1430. <https://doi.org/10.1126/science.1148841>.
- 731 (61) Il'ichev, Y. V.; Perry, J. L.; Simon, J. D. Interaction of Ochratoxin A with Human Serum Albumin.
732 Preferential Binding of the Dianion and PH Effects. *J. Phys. Chem. B* **2002**, *106* (2), 452–459.
733 <https://doi.org/10.1021/jp012314u>.
- 734 (62) Gao, T.; Zhang, W.; Wang, Y.; Yang, G. DNA Compaction and Charge Neutralization Regulated by
735 Divalent Ions in Very Low PH Solution. *Polymers* **2019**, *11* (2), 337.
736 <https://doi.org/10.3390/polym11020337>.
- 737 (63) Saha, M.; Nandy, P.; Chakraborty, M.; Das, P.; Das, S. The Importance of PKa in an Analysis of
738 the Interaction of Compounds with DNA. *Biophysical Chemistry* **2018**, *236*, 15–21.
739 <https://doi.org/10.1016/j.bpc.2018.02.001>.
- 740 (64) Miller, B. S.; Bezing, L.; Gliddon, H. D.; Huang, D.; Dold, G.; Gray, E. R.; Heaney, J.; Dobson, P. J.;
741 Nastouli, E.; Morton, J. J. L.; McKendry, R. A. Spin-Enhanced Nanodiamond Biosensing for
742 Ultrasensitive Diagnostics. *Nature* **2020**, *587* (7835), 588–593. [https://doi.org/10.1038/s41586-](https://doi.org/10.1038/s41586-020-2917-1)
743 [020-2917-1](https://doi.org/10.1038/s41586-020-2917-1).
- 744 (65) Zhao, L.; Nakae, Y.; Qin, H.; Ito, T.; Kimura, T.; Kojima, H.; Chan, L.; Komatsu, N. Polyglycerol-
745 Functionalized Nanodiamond as a Platform for Gene Delivery: Derivatization, Characterization,
746 and Hybridization with DNA. *Beilstein J Org Chem* **2014**, *10*, 707–713.
747 <https://doi.org/10.3762/bjoc.10.64>.
- 748 (66) Petrakova, V.; Benson, V.; Buncek, M.; Fiserova, A.; Ledvina, M.; Stursa, J.; Cigler, P.; Nesladek,
749 M. Imaging of Transfection and Intracellular Release of Intact, Non-Labeled DNA Using
750 Fluorescent Nanodiamonds. *Nanoscale* **2016**, *8* (23), 12002–12012.
751 <https://doi.org/10.1039/C6NR00610H>.
- 752
- 753